American Mineralogist, Volume 88, pages 1919–1932, 2003

Efflorescent iron sulfate minerals: Paragenesis, relative stability, and environmental impact

JEANETTE K. JERZ* AND J. DONALD RIMSTIDT

Department of Geological Sciences, Virginia Polytechnic Institute and State University, Blacksburg, Virginia 24061, U.S.A.

ABSTRACT

This study of a pyrrhotite-dominated massive sulfide deposit in the Blue Ridge province in southwestern Virginia shows that sulfate minerals formed by the oxidation of the pyrrhotite transform from one to another by a combination of oxidation, dehydration, and neutralization reactions. Significant quantities of sulfate minerals occur in the underground adits (Area I) and under overhangs along the high sidewall of the adjoining open pit (Area II). Samples from this site were analyzed to determine mineralogy, equilibrium relative humidity, chemical composition, and acid generation potential. In Area I, pyrrhotite oxidizes to marcasite + melanterite, which eventually oxidizes to melanterite + sulfuric acid. Melanterite is extruded from the rocks as a result of the volume change associated with this reaction. It accumulates in piles where halotrichite, copiapite, and fibroferrite form. In Area II, $FeSO_4$ solutions produced by pyrrhotite oxidation migrate to the exposed pit face, where they evaporate to form melanterite. The melanterite rapidly dehydrates to form rozenite, which falls into a pile at the base of the wall, where melanterite, copiapite, and halotrichite are present. The observed paragenesis can be understood using a $\log a_{O_2} - \log a_{H_2O}$ diagram that we developed from published thermodynamic data and observations of coexisting phases.

Dissolution experiments showed that fibroferrite-rich samples had the highest acid producing potential, followed by copiapite-rich samples and then halotrichite-rich samples. The most abundant metals in solutions produced by dissolving impure bulk samples of the salts were Mg, Al, Zn, Cu, Ca, and Pb. The molar concentrations of the metals varied with mineralogy. However, all of the sulfate minerals release metals and acid when they dissolve and therefore represent a potentially significant environmental risk.

INTRODUCTION

Acid mine drainage (AMD) environments provide of a rich tapestry of mineralogy and geochemistry. Although the heterogeneity and complexity of AMD systems can make them difficult to study, we expect them to show a systematic pattern of mineral paragenesis. Knowledge of this paragenesis is important for quantifying the environmental impact of the minerals, predicting the evolution of AMD sites, and identifying effective AMD remediation methods. A first step toward addressing the paragenesis problem is to consider only reactions involving the most important AMD elements: iron, sulfur, oxygen, and hydrogen. The important acid mine drainage minerals can be divided into three types: iron sulfides, iron sulfates, and iron oxyhydroxides. The overall AMD-forming process involves a complex chain of reactions that link the oxidation of iron sulfides to the precipitation of iron oxyhydroxides and the release of sulfuric acid to receiving waters. For pyrite and marcasite, the overall reaction is:

$$FeS_2 + \tfrac{15}{4}O_2 + \tfrac{7}{2}H_2O = Fe(OH)_3 + 2H_2SO_4 \quad (1)$$

and for pyrrhotite the overall reaction is:

$$Fe_{1-x}S + \tfrac{9-3x}{4}O_2 + \tfrac{5-x}{2}H_2O = (1-x)Fe(OH)_3 + H_2SO_4 \quad (2)$$

Iron sulfide and iron oxyhydroxide geochemistries have been well studied (see Nordstrom and Alpers 1999 and references therein), but the equally important iron sulfate phases are less well understood. The objective of this study is to establish the geochemical relationships of some important iron sulfate minerals that occur in AMD environments.

Numerous hydrated iron sulfate minerals are known (Table 1), and their mineralogy and geochemistry are discussed in a recent review by Jambor et al. (2000). Efflorescent iron sulfate minerals are common in base metal deposits, coal deposits, and tailings and waste rock piles where they are frequently associated with oxidizing iron sulfide minerals. Because of their high solubility, most iron sulfate minerals only persist under rock overhangs and similar sheltered sites where they are protected from dissolution during rain events. The minerals can also form in the open during drier times as sulfate-rich solutions migrate to the surface and evaporate.

These iron sulfate minerals form when solutions rich in iron sulfate and in sulfuric acid evaporate in surficial environments. The evolution from ferrous sulfate minerals to iron oxyhydroxide minerals occurs by a series of oxidation, dehydration, and neutralization reactions. The mineralogy that develops at any particular site will be controlled by the relative rates of each of these types of reactions. We can predict the order in which the minerals in Table 1 are likely to form by

* Present address: Department of Geology and Geography, DePauw University, 602 South College Avenue, Greencastle, Indiana 46135, U.S.A. E-mail: jjerz@depauw.edu

examining their stoichiometries in terms of these three reaction types. The axes of Figure 1, based on the atomic ratios of chemical constituents, are designed to show how the minerals are related by oxidation, neutralization, and dehydration reactions. The oxidation axis expresses the amount of cationic charge provided by ferric iron divided by the total cationic charge. This number increases when ferrous iron oxidizes to ferric iron. The neutralization axis expresses the ratio of anionic charge provided by hydroxide to the total charge provided by all anions. This number increases as minerals incorporate hydroxide from solution or as sulfate is lost to solution as H_2SO_4. The dehydration axis expresses the number of moles of water molecules per total moles of cationic charge. This ratio decreases as water is lost by dehydration. The bold arrow shows the general trend of compositions as ferrous sulfates evolve to iron oxyhydroxides. The diagram explains why minerals such as lausenite (lau) are rare in AMD environments; they can form only under strongly acidic conditions. More common minerals, such as copiapite (cop), fall near the most direct path leading from melanterite (mel) to goethite (goe). By examining the geochemistry, mineralogy, and occurrence of these phases, we can begin to map out the important reactions that result in the overall transformation processes.

TABLE 1. Minerals that occur in the system Fe-S-O-H

Name and abbreviation		Formula
hematite	hem	$Fe_2^{3+}O_3$
goethite	goe	$Fe^{3+}OOH$
hydrous ferric oxide*	hfo	$Fe^{3+}(OH)_3{\cdot}nH_2O$
maghemite†	mhem	$Fe_2^{3+}O_3$
quenstedtite	quen	$Fe_2^{3+}(SO_4)_3{\cdot}10H_2O$
coquimbite	coq	$Fe_2^{3+}(SO_4)_3{\cdot}9H_2O$
paracoquimbite‡	pcoq	$Fe_2^{3+}(SO_4)_3{\cdot}9H_2O$
kornelite	korn	$Fe_2^{3+}(SO_4)_3{\cdot}7H_2O$
lausenite	laus	$Fe_2^{3+}(SO_4)_3{\cdot}6H_2O$
hohmannite	hoh	$Fe_2^{3+}(SO_4)_2(OH)_2{\cdot}7H_2O$
metahohmannite	mhoh	$Fe_2^{3+}(SO_4)_2(OH)_2{\cdot}3H_2O$
fibroferrite	fib	$Fe^{3+}(SO_4)(OH){\cdot}5H_2O$
amarantite	amar	$Fe^{3+}(SO_4)(OH){\cdot}3H_2O$
butlerite	but	$Fe^{3+}(SO_4)(OH){\cdot}2H_2O$
parabutlerite	pbut	$Fe^{3+}(SO_4)(OH){\cdot}2H_2O$
bilinite	bil	$Fe^{2+}Fe_2^{3+}(SO_4)_4{\cdot}22H_2O$
römerite	röm	$Fe^{2+}Fe_2^{3+}(SO_4)_4{\cdot}14H_2O$
copiapite	cop	$Fe^{2+}Fe_4^{3+}(SO_4)_6(OH)_2{\cdot}20H_2O$
ferricopiapite	fcop	$Fe_5^{3+}O(SO_4)_6OH{\cdot}20H_2O$
melanterite	mel	$Fe^{2+}SO_4{\cdot}7H_2O$
ferrohexahydrite	fhex	$Fe^{2+}SO_4{\cdot}6H_2O$
siderotil	sid	$Fe^{2+}SO_4{\cdot}5H_2O$
rozenite	roz	$Fe^{2+}SO_4{\cdot}4H_2O$
szomolnokite	szo	$Fe^{2+}SO_4{\cdot}H_2O$
rhomboclase	rhom	$H_3OFe^{3+}(SO_4)_2{\cdot}3H_2O$
hydronium jarosite	h-jar	$H_3OFe_3^{3+}(SO_4)_2(OH)_6$
schwertmannite	sch	$Fe_{16}^{3+}O_{16}(OH)_{12}(SO_4)_2$

Note: Not all of these minerals are found in the AMD environment. The abbreviations are used in subsequent figures and tables in this paper.
* A complex group of phases that includes ferrihydrite and lepidocrocite.
† Polymorph of hematite.
‡ Polymorph of coquimbite.

Knowledge of the sulfate mineralogy and paragenesis at an AMD site is important because different sulfate minerals carry different amounts of trace elements and produce different amounts of acid upon dissolution. The dissolution of iron sulfate minerals during rain events can dramatically affect aquatic ecosystems. Dagenhart (1980) showed a clear relationship between stream discharge and stream chemistry during rain events (Fig. 2). His data show that during the initial phase of a rain

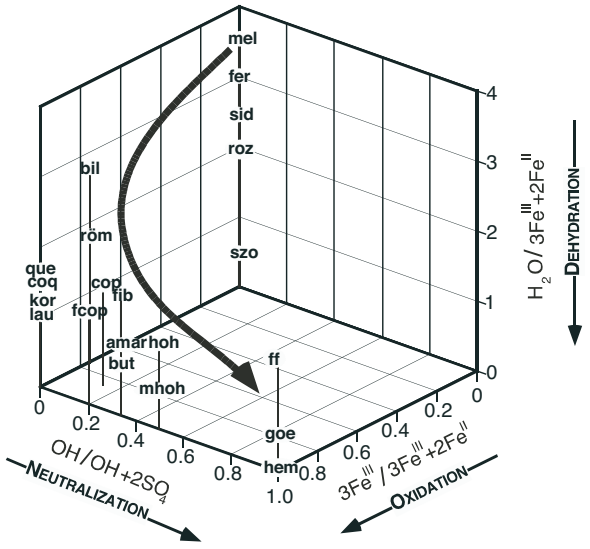

FIGURE 1. The stoichiometries of iron sulfate and iron oxide minerals are directly related to the reactions that transform one phase into another. Mineral stoichiometries and abbreviations are given in Table 1. Changes in the ratios along the axes correspond to chemical reactions that are responsible for iron sulfate mineral transformations in acid mine drainage environments. These reactions are dehydration (z-axis), neutralization (y-axis), and oxidation (x-axis). The bold line shows a generalized paragenesis path involving these three reactions that converts ferrous sulfate to iron oxyhydroxides.

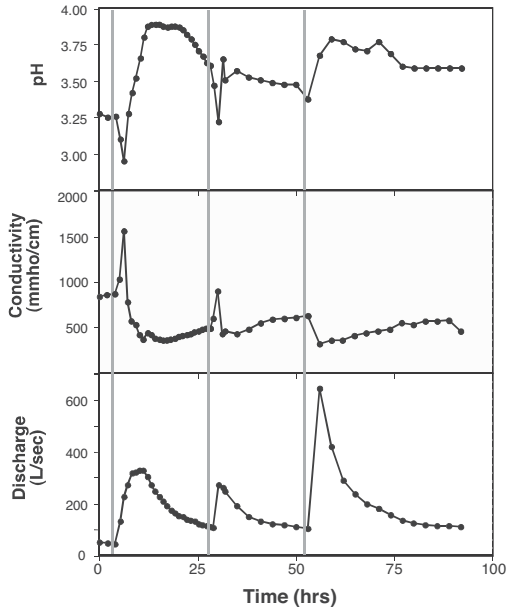

FIGURE 2. Hydrograph of Contrary Creek, Virginia, showing the relationship between stream discharge and stream chemistry for rain events in June, 1978 (Dagenhart 1980). The bold vertical lines represent rain events. Runoff from the first storm event dissolved sulfate minerals and carried the resulting acidic, sulfate-rich solution to the stream, causing an increase in acidity and conductivity. After a short time, relatively fresher water from upstream diluted the stream. Later storm events produce smaller excursions in conductivity and pH because the sulfate minerals had been previously washed away.

event, there was a marked decrease in pH and an increase in dissolved solids as iron sulfate minerals dissolved and the acid sulfate solutions were carried by overland flow into the stream. With time, the pH rose and the dissolved solids declined as the water draining the sulfate rich area was diluted by cleaner water from upstream. During a later storm event, no significant change in water chemistry was observed because the soluble sulfates had been washed away by the earlier events. Bayless and Olyphant (1993) and Alpers et al. (1994) documented changes in sulfate mineral chemistry as a result of wet and dry periods. Keith et al. (1999, 2001) reported that iron sulfate minerals accumulate during dry periods and that their rapid dissolution during the first rain in the wet season released high concentrations of metals into local streams. In addition, they noted that the degree of trace element and acid release could be related to the mineralogy of the iron sulfates. Stewart et al. (1997) observed similar effects using leaching columns in a laboratory setting. They found that coal wastes with a 4% pyritic sulfur content produced enhanced acidity and iron and sulfate concentrations when the columns were leached after long periods of drying during which efflorescent salts had formed. These laboratory and field studies provide evidence that the dissolution of iron sulfates can rapidly contribute acid and metals to receiving waters.

Another effect of the dissolution of iron sulfate minerals is the promotion of pyrite oxidation. Ferric iron oxidizes pyrite faster in aqueous systems than dissolved oxygen does (McKibben and Barnes 1986; Williamson and Rimstidt 1994). However, at low pH, the oxidation rate of ferrous iron is slow (Singer and Stumm 1970). The dissolution of sulfate minerals rich in ferric iron near the top of waste piles can release ferric iron solutions that will infiltrate the wastes where they will cause pyrite oxidation at deep levels where oxygen cannot penetrate. Therefore, the dissolution of ferric sulfate minerals creates a positive feedback mechanism for the further generation of AMD (Cravotta 1994).

There have been several field and laboratory studies of sulfate mineral paragenesis (Bandy 1938; Bol'shakov and Ptushko 1971; Zodrow et al. 1979; Nordstrom and Alpers 1999; Frau 2000). Generally, iron sulfate minerals have been observed to evolve from all ferrous iron to mixed ferrous/ferric iron to all ferric iron phases and to dehydrate via the loss of structural water. Jambor et al. (2000) compared the results of some field and laboratory paragenetic sequences as summarized in Table 2.

TABLE 2. Observed paragenesis of sulfate minerals (from Jambor et al. 2000)

	Alcaporrosa, Chile Bandy (1938)	Laboratory Buurman (1975)	Iron Mountain, CA Nordstrom and Alpers (1999)
early	pyrite	pyrite	pyrite
		melanterite	
		siderotil	
		rozenite	rozenite
	szomolnokite	szomolnokite	szomolnokite
	römerite	rhomboclase	copiapite
	quenstdtite		römerite
	coquimbite	coquimbite	coquimbite
	pickeringite	römerite	kornelite
	copiapite		rhomboclase
	parabutlerite	voltaire	voltaite
late	jarosite		halotrichite-billinite

This paper builds on the results of these previous studies of the paragenesis of sulfate minerals and their environmental impact. Its purpose is to report our analysis of the paragenesis of sulfate minerals occurring at a pyrrhotite-dominated massive sulfide deposit, based on our interpretation of the thermodynamic stability of the iron sulfate minerals. In addition, we evaluate some aspects of the environmental impact of the minerals found at this site.

METHODS

The field site for this study is a disused mine located in the Blue Ridge province in southwestern Virginia (Fig. 3). The mine is at the southern end of the Great Gossan Lead, which is a 28 km-long, discontinuously mineralized zone that trends to the northwest from a point approximately 6 km north of Galax, Virginia to 10 km north of Hillsville, Virginia. The Gossan Lead consists of irregular pods and vein-like bodies of massive pyrrhotite, the long dimensions of which are approximately parallel to the NNE-SSW foliation of the host rocks (Stose and Stose 1957; Henry et al. 1979). A comprehensive review of the economic geology of the Gossan Lead is given in Gair and Slack (1984).

The Gossan Lead is part of the Precambrian Ashe Formation, which consists of fine-grained sulfidic metagraywacke, gritty metagraywacke, and sulfidic to graphitic phyllite (Rankin et al. 1973). Staten (1976) reported that the Gossan Lead part of the Ashe Formation is mostly made up of quartz-muscovite schist and gneiss, with minor amounts of hornblende gneiss and amphibolite, biotite to chlorite schists, biotite-chlorite gneiss, and calcareous rock. Gair and Slack (1984) preferred the term granofels rather than gneiss because the rocks in the vicinity of the massive sulfide deposits lack the typical layering of high-grade metamorphic rocks. The primary sulfide minerals are pyrrhotite (more than 90% of the sulfide mass) with minor sphalerite and chalcopyrite (Staten 1976; Henry et al. 1979; Craig 1980). Henry et al. (1979) identified the pyrrhotite to be the intermediate hexagonal variety ($Fe_{0.9}S$). Pyrite is very rare to absent in most of the Gossan Lead, but increases in abundance toward the Betty Baker mine in the northeast. Additional ore minerals reported by Henry et al. (1979) include trace amounts of galena, arsenopyrite, cubanite, mackinawite, tetrahedrite, stannite, native bismuth, rutile, ilmenite, and graphite. The samples and field observations made for this study were from the Bumbarger open pit and the adjacent subsurface Iron King mines in the Iron Ridge segment of the Great Gossan Lead. Iron Ridge is at the southwestern end of the Gossan Lead, approximately 6 km north of Galax, Virginia. The Iron Ridge segment was the only area of the Gossan Lead that was mined for primary sulfides, and the deposits are the only ones that have been mined since 1908 (Gair and Slack 1984).

FIGURE 3. Location of the Great Gossan Lead in Virginia (shaded), U.S.A.

This segment is 2 km long and contains three mine sites: the Huey, the Gossan Howard, and the Bumbarger plus Iron King complex.

In 1998, the entrance to the Bumbarger mine was regraded and some of the tailings were removed. However, the Bumbarger pit and Iron King adits have not been remediated and therefore the most of the mine was accessible. We chose to sample from the Bumbarger-Iron King mine because we could gain access, because the mining history, ore mineralogy, and economic geology of the area have been documented (Stose and Stose 1957; Henry et al. 1979; Gair and Slack 1984), and because there is an abundance of sulfate minerals available for study. The Bumbarger mine was mapped and described by Gair and Slack (1984). The pit is oblong, approximately 100×60 m, and is 40 m deep. A birdfoot-shaped bench divides the pit into three sections. In 1935, several adits were driven to the Iron King portion of the deposit (Henry et al. 1979). The portal areas are dark, cool, and damp.

The water content of the pit varies by season. The annual precipitation for the area is approximately 91 cm and the average temperature highs and lows are 28 and –6 °C, respectively. Two pools of AMD occur on the floor of the Bumbarger mine. One is ephemeral and one is permanent. The permanent pool is in the deepest part of the pit near an underground opening. The Iron King adits have a higher relative humidity than the open area of the Bumbarger mine. Water drips from the roof of the adits year-round, but water flow is insufficient to dissolve the sulfate minerals that are present.

Significant quantities of sulfate minerals were found in the Iron King adits (Area I) and under overhangs along the high sidewall of the Bumbarger pit (Area II). Sampling locations for Areas I and II are indicated on Figure 4. At each site, trenches were made through representative piles. Samples were collected from the wall or roof, the surfaces of the piles, and at various depths in each trench. The samples were collected during several trips during the summer of 2001.

Samples brought back to the laboratory were analyzed to determine mineralogy, equilibrium relative humidity, chemical composition, and acid generation potential. Samples were stored in air-tight bags and analyses commenced soon after collection to minimize mineralogy changes in response to the environmental conditions in the laboratory.

Each sample was subsampled on the basis of visual differences, primarily color, using a binocular microscope. Most of the samples were very fine grained, and it was nearly impossible to isolate pure individual minerals. However, using this method, subsamples consisting of a few predominant minerals were obtained.

The mineralogy of the subsamples was identified using X-ray diffractometry (XRD) with Cu$K\alpha$ radiation. Samples were ground with an agate mortar and pestle, suspended in benzene, and mounted on zero-background quartz plates. Each sample was scanned between 4 and 80° 2θ at a scan rate of 1° per minute. Selected samples were reanalyzed to determine if the mineralogy changed upon sample aging. Identification was done by comparing the diffraction pattern of the unknown against patterns for known minerals listed in the Powder Diffraction File (PDF 2000).

In addition to XRD analysis of the mineral separates, bulk samples and insoluble fractions were analyzed in powder mounts using the same XRD conditions as for the sulfate mineral separates. These patterns were compared to the sulfate mineral patterns to refine the identification. Interpretation of many of the X-ray diffraction patterns was difficult because of the mineralogical complexity of the samples. Therefore, optical microscopy and scanning electron microscopy (SEM) with energy dispersive spectroscopy (EDS) for elemental analysis were used to assist in the mineral identifications.

Nearly all iron sulfate minerals are hydrous. The number of waters of hydration, and therefore the mineralogy, is controlled by relative humidity and temperature. To determine the equilibrium relative humidity of selected subsamples, we used a modified version of the humidity buffer method of Chou et al. (2002). In this method, samples were placed in humidity-buffered chambers and changes in sample weight were recorded over time. The humidity buffers are based on various saturated salt solutions (Table 3), which were prepared by placing 30 g of the salt and 5 g of water into a plastic vial. This amount was sufficient to create a saturated solution with some solid present.

When solutes are added to water the a_{H_2O} is reduced from a value of 1.0 (pure water) and the partial pressure of water in the vapor phase decreases proportionally to a_{H_2O} in solution. In this paper, we use pure liquid water as a reference state ($a_{H_2O} = 1.0$) so that the relative humidity (100%) can be directly compared with the activity of water in solution (relative humidity = $a_{H_2O} \times 100\%$). Note that Chou et al. (2002) use ideal water vapor at 1 bar pressure as a reference state. These two reference states are related through the reaction:

$$H_2O_{(l)} = H_2O_{(v)} \quad (3)$$

which has a log K = –1.4991. This means that the partial pressure of pure water at 25 °C is 0.031691 bar (Haar et al. 1984). These two reference states can be compared by considering a saturated solution of $CuSO_4 \cdot 5H_2O$ at 298 K, where $a_{H_2O} = 0.972$ (pure liquid water reference state) and the vapor pressure of water, P_{H_2O}, in equilibrium with this solution is (0.972)(0.031691) bar. This means that $a_{H_2O} = 0.972$ (pure, liquid water reference state) corresponds to $a_{H_2O} = 0.029941$ (ideal water vapor at 1 bar reference state). For a saturated salt solutions, the concentration of the salt is fixed by equilibrium with the solid. This means that a_{H_2O} in the solution is fixed. If a vapor phase is in equilibrium with this solution the activity of water (expressed as relative humidity) must equal the activity of water in the saturated solution. In our experiments, if the sample absorbed water from the vapor, water evaporated from the solution causing salt to precipitate so as to keep the solution concentration constant. On the other hand, if the sample released water to the vapor, it was absorbed by the salt solution, which lowered the concentration of dissolved salt and caused some salt to dissolve.

Two grams each of the field samples that contained a sulfate phase of interest were placed inside a preweighed glass sample vial (Fig. 5). The sample vial was then placed inside a second glass vial in the humidity buffer container. The second glass vial kept the sample vial from contacting the saturated salt solution. The container was sealed and placed in a constant temperature bath set to 25 °C. The sample vial was removed from the cell and reweighed after 7–10 days, when the weight change pattern for the minerals had been established.

Graphs of the weight change vs. the buffered relative humidity for each sample showed whether samples had gained weight by absorbing water from the atmosphere inside the sealed container or lost weight as the sample dehydrated. The point at which the sample neither gained nor lost weight was selected as the sample's equilibrium relative humidity, i.e., the point on the graph where the weight change curve crossed the x-axis.

For example, Figure 6 shows a graph of weight change vs. relative humidity for the sample that was dominantly fibroferrite (third graph from top). At

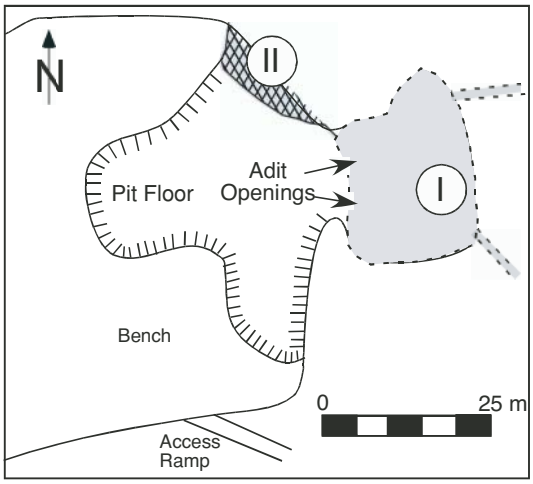

FIGURE 4. Map of a portion of the Bambarger-Iron King mines in the Iron Ridge segment of the Gossan Lead. The two sampling areas, I and II, are indicated on the map. The dashed line around area I indicates the boundary of the underground workings. The crosshatching at area II indicates the overhang of the side-wall.

TABLE 3. Salts used to make saturated solution for humidity buffer method (Young 1967; Greenspan 1977)

Saturated Solution	Relative Humidity
$CuSO_4 \cdot 5H_2O$	97.20%
$BaCl_2 \cdot 2H_2O$	90.30%
$(NH_4)_2SO_4$	80.20%
$SnCl_2 \cdot 6H_2O$	70.85%
$CoCl_2$	64.92%
$NaBr \cdot 2H_2O$	58.20%
$Mg(NO_3) \cdot 6H_2O$	52.82%

Note: The relative humidity values are reported for 25 °C.

high relative humidity (97%), the sample absorbed water from the atmosphere and deliquesced. At lower relative humidities (all buffers lower than 80%), the sample lost weight through drying of the adhering iron sulfate-sulfuric acid solution. At a relative humidity of 88%, the sample neither gained nor lost weight. Therefore, fibroferrite and the coexisting iron sulfate-sulfuric acid solution are stable in atmospheres that have a relative humidity at or near 88%.

Previous workers noted that the dissolution of the sulfate minerals during rain events produces acidic, trace element-enriched sulfate solutions that can dramatically degrade receiving waters (Dagenhart 1980; Bayless and Olyphant 1993; Jerz 1998). We performed dissolution experiments of field-gathered samples to determine their acid generation and metal release potential.

For each experiment, a known weight of sample was dissolved in a known volume of deionized water in a preweighed, acid-washed centrifuge tube. Specific water:mineral ratios varied depending on the amount of sample available, but were typically 100 mL:15 g. The solutions were stirred for 1 minute before the tubes were centrifuged at 158 × g (g = 9.81 m/s^2) for 10 minutes and decanted into an acid-washed beaker. The residium was dried and weighed to determine the amount of insoluble material in each sample and the pH of the supernatent was measured. A 10 mL aliquot of the supernatent was diluted 1:5 in a 50 mL volumetric flask and the pH of this diluted sample was measured. Then a 10 mL aliquot of this diluted supernatent solution was diluted 1:5 and the pH of the resulting 1:25 dilution was measured. This serial dilution and pH measurement procedure was repeated a total of ten times. Half of the most dilute sample was acidified with HCl and saved for Inductively Coupled Plasma (ICP) analysis.

Similar dissolution experiments were performed to determine the metal concentrations of the samples. Known weights of samples were allowed to dissolve in 50 mL of deionized water for 30 minutes before the samples was centrifuged at 158 × g for 10 minutes and decanted into an acid-washed beaker. The residium was dried and weighed to determine the amount of dissolved material. The concentration of Na, Mg, Si, P, S, K, Ca, Cr, Mn, Fe (total), Co, Ni, Cu, Zn, Pb, Cd, and Al was measured by ICP-AES within a week of their extraction. We assumed that all of the sulfur detected was in the form of sulfate. Ferrous and ferric iron content was estimated by assuming charge balance.

RESULTS

Area I is in a large, cavernous adit. The roof is more than seven meters above the adit floor near the opening from the pit and slopes to a height of approximately three meters at the back wall, although it is lower in some places. It is approximately 35 meters across and 20 meters from the opening from the pit to the back wall and several narrow tunnels extend much further. The surface of the adit floor is hummocky and most of the floor is covered by sulfate minerals, either in piles or in a veneer. In a few places there is standing water or desiccation cracks in an iron oxide mud, suggesting that pools of water have evaporated. Rarely, bedrock is exposed on the floor. In several places, iron oxyhydroxide stalactites hang from the roof, mostly above areas of standing water.

There are several piles of sulfate minerals in Area I (Fig. 7). These appear to have formed beneath pyrrhotite rich zones or pods in the roof. The piles range in size from a meter or less across to several meters across and up to 1.5 meters deep. The sulfate minerals in the piles are moist to wet. The particles in the piles range in size from a few centimeters in diameter to mostly less than a millimeter. In addition, large pieces (>20

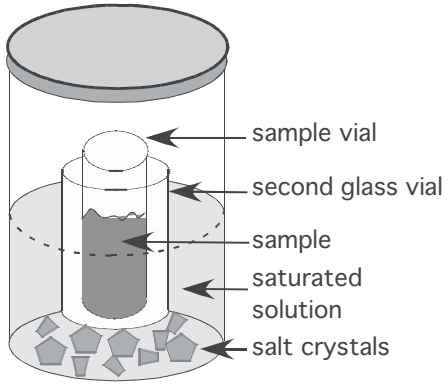

FIGURE 5. Schematic of humidity-buffer method. The relative humidity (a_{H_2O}) in the sealed container is buffered by the saturated salt solutions listed in Table 3. Field samples were placed in a glass sample vial inside the chamber.

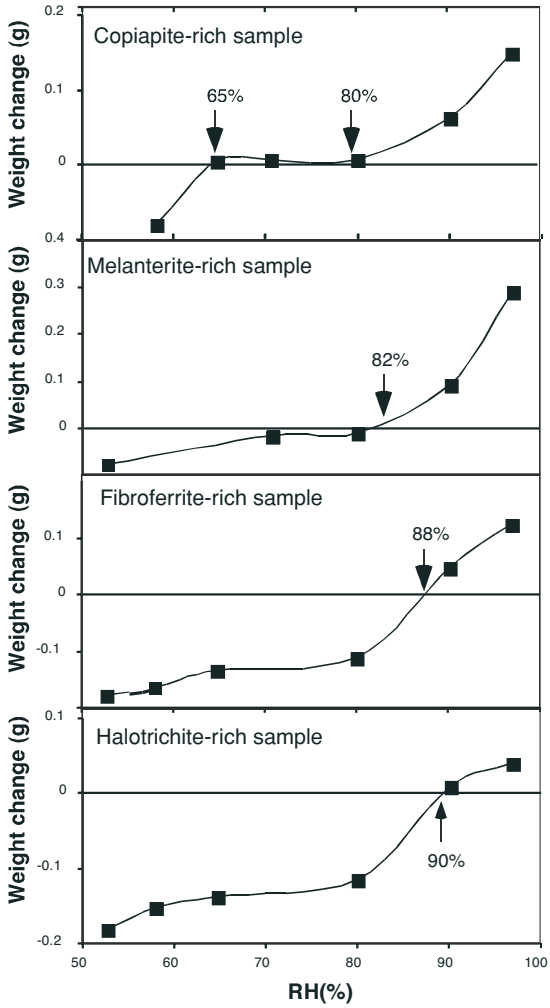

FIGURE 6. Example of the data collected with the humidity buffer method. The change in the weight of the a 2 gram sample equilibrated with a vapor phase of fixed RH for 7 days was plotted versus the relative humidity. Samples that gained weight absorbed water from the vapor phase; samples that lost weight dehydrated and released water to the vapor phase. The intersection of the line with x-axis (change in weight = 0) is the relative humidity at which the sample is stable. The melanterite, halotrichite and fibroferrite samples were damp (as collected from the field). Therefore, part of the weight loss for these samples in the low RH experiments is due to the evaporation of these solutions. Each square represents one of the relative humidity buffers listed in Table 3

cm) of wall rock have fallen and been buried in the piles. The mineralogy of the piles is highly heterogeneous, consisting of mixed sulfate, silicate, sulfide, and iron oxyhydroxide phases. Efflorescent blooms of sulfate minerals occur around the bases of most piles. These blooms are moist and in some cases appear to contain some flow structure. The color of these blooms fluctuated during our numerous visits to this site, suggesting that their mineralogy changes with environmental conditions.

Area II is located on the sidewall of the pit, a few meters to the northeast of the opening to Area I. It has good sun exposure and is usually warm and dry. Sulfate minerals occur beneath an overhang in the side-wall. The sulfate minerals are distinctly different in Area II; they occur as encrustations or efflorescent blooms, which are usually dry and porous. Many fine "hair salts" coat the surfaces of exposed rocks on the ground or the sulfate blooms. Underneath the top layer, minerals are highly friable and fine grained. Fine-grained sulfate minerals also occur on the surface of the side wall. We have also observed that the color of the sulfate minerals at Area II fluctuates over time.

The minerals identified from the field site and a description and the location of each are listed in Table 4. Most of the samples consisted of a mixture of phases. Our efforts were focused on identifying the dominant sulfate minerals present in the samples. The minerals are not pure, end-member phases. In addition to sulfate phases, we were able to identify some other minerals, but a detailed mineralogical investigation of the paragenesis of the other phases was not a goal of this study.

Field samples were used in the relative humidity experiments. Although the samples were selected so they contained predominantly one mineral, other sulfate, silicate, and oxyhydroxide phases were present. Furthermore, some of the samples were damp because of the presence of ferrous sulfate-sulfuric acid solutions. The results presented here represent the relative humidity where each of these complex samples would be stable relative to the predominant hydration/dehydration reactions. The equilibrium relative humidity over the pure, end-member minerals are likely to be different than reported for these samples.

The results of the humidity buffer experiment are shown in Figure 6. The fibroferrite-rich sample was found to deliquesce at relative humidities greater than 88%. The halotrichite-rich sample was found to deliquesce at relative humidities greater than 90%. The copiapite-rich sample was found to deliquesce at a relative humidity greater than 80%. Copiapite was found to be stable (i.e., not dehydrate) to a relative humidity of 65%. The melanterite-rich sample was found to deliquesce at relative humidities greater than 82%; note that this is lower than the relative humidity (96%) for a solution saturated with pure melanterite (Apelblat 1993).

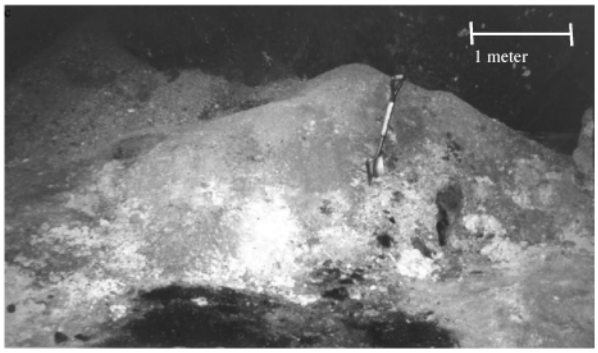

FIGURE 7. Large pile of predominantly sulfate minerals from area I at the field site. The dimensions of the pile are approximately 2.5 meters long, 1.5 meters wide, and 1.25 meters deep.

The acid-producing potential of each field sample is illustrated by graphs of pH vs. weight percent sample dissolved (Fig. 8). Tables of the data used to construct these graphs are found in Jerz (2002). Fibroferrite-rich samples had the highest acid-producing potential, followed by copiapite-rich samples and then halotrichite-rich samples. Melanterite-rich samples had the lowest acid producing potential.

Pie charts showing the concentrations of some important elements in selected samples (Fig. 9) were made by dividing the molar concentration of each metal by the sum of the molar concentrations of all metals. Tables of the data used to construct these charts are found in Jerz (2002). For most samples, iron was the dominant metal released upon dissolution. The minor and trace element concentrations can vary significantly between sample types. This suggests that the processes that transform one sulfate mineral to another also redistribute these minor and trace elements.

The relative dissolution rates of the sulfate minerals were estimated by weighing the dried, residual material left in the centrifuge tubes after the dissolution experiments. Melanterite, copiapite, and halotrichite had relatively high dissolution rates, and the dissolution rate of fibroferrite was slower.

Mineral relationships in the field

Our observations of the iron sulfate mineralogy at the field site provide a reference case that can be used to understand the paragenesis of sulfate minerals from pyrrhotite-dominated massive sulfide deposits. The paragenesis that we observed is consistent with the stability of various sulfate phases and can be best understood using a $\log a_{O_2} - \log a_{H_2O}$ diagram that we created on the basis of published thermodynamic values and the results of our experiments. Our knowledge of this paragenesis sets the stage for understanding the environmental impact of iron sulfate minerals because the evolving sulfate mineralogy affects the acid and trace element load of runoff solutions.

The paragenesis of the iron sulfate minerals at each field site can be broken down into three steps (Fig. 10). The temperature and relative humidity of the two sites are different so that the paragenesis path at each site is different. However, we can combine the observations from both sites to create a general paragenesis model for the pyrrhotite dominant system. Note that because of kinetic constraints minerals often persist beyond the range of their thermodynamic stability. This means that the activity diagrams are most useful for determining the first appearance of a phase but are not particularly useful for predicting the disappearance of a phase.

At Area I, the first step in the paragenesis is the oxidation of pyrrhotite in the roof rocks to create melanterite and sulfuric acid.

$$Fe_{1-x}S + \tfrac{8-2x}{4}O_2 + (7 + x)H_2O = (1-x)FeSO_4 \cdot 7H_2O + xH_2SO_4 \quad (4)$$

TABLE 4. Description of the minerals found at the Bumbarger-Iron King mine (see Fig. 4 for the location of areas I and II)

Mineral	Description	Location
melanterite	Elongate, curved blue green crystals	I: in roof and pile II: bottom of trench
rozenite	Very fine grained, white crystals	II: along sidewall, in pile
halotrichite	Fibrous, white masses of (area I) or single (area II) crystals	I: in pile II: at surface
copiapite	Pale yellow to orange efflorescent blooms; moist and waxy in area I, dry in area II.	I: in pile; along the sides of pile II: at surface
fibroferrite	Moist, yellow brown efflorescent blooms; some times masses appeared to contain flow structure	I: along the side of pile
Other sulfates	minor jarosite, römerite possible	
Sulfides	Pyrrhotite and pyrrhotite altered to FeS_2; chalcopyrite	I & II: several places at site
Silicates	Altered actinolite, mica, quartz	I & II: several places at site
Iron oxides	Earthy; amorphous and fine grained	I & II: several places at site

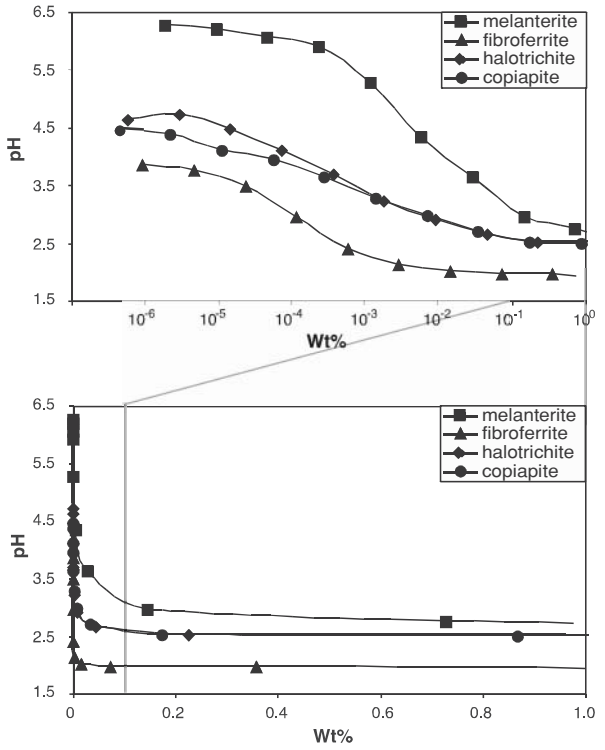

FIGURE 8. Graphs of pH versus weight percent mineral dissolved in solution for selected field samples (dominant mineralogy listed in the legends). The x-axis on the top graph is presented on a logarithmic scale to show the behavior in very dilute solutions.

In addition, some marcasite forms from the oxidative leaching of pyrrhotite. Some of the sulfuric acid reacts with surrounding silicate or other sulfide minerals to release other cations (e.g., Al^{3+}, Zn^{2+}) into solution. Melanterite produced by this reaction has a much larger molar volume than pyrrhotite [V_m (pyrrhotite) = 16.88 cm^3/mol, V_m (melanterite) = 146.56 cm^3/mol] (Robie and Hemmingway 1995). The melanterite crystals found in the roof were curved and anhedral, which is consistent with the idea that they were extruded into available pore space as they formed. In the second step, the extruded melanterite along with silicate minerals and unreacted sulfide minerals fall to the floor and accumulate into piles. The melanterite continues to oxidize and ferric iron precipitates resulting in a thin film of Fe^{2+}-Fe^{3+}-H^+-SO_4^{2-} solution on the grains in the pile. In the third step, ferrous sulfate-sulfuric acid solutions drip from the roof onto the pile and this solution combines with the solution film on the grains and migrates to areas where evaporation causes new minerals to grow as efflorescent blooms. The minerals were identified as copiapite, fibroferrite, or halotrichite. The specific mineral that forms is a function of the local solution composition, relative humidity, and degree of oxidation. Fibroferrite was found when the relative humidity was high, whereas copiapite occurred under drier conditions. Halotrichite was found both in the pile and buried in the material that covered the floor of the adit. In our laboratory experiments, halotrichite was found to be stable at high relative humidities. However, it may precipitate at late stages in the paragenesis because the activity of aluminum becomes high relative to iron as the dissolved iron is removed through the formation of iron sulfate minerals.

At Area II, most of the primary material had been oxidized and fresh pyrrhotite was not exposed at the surface of rock. However, polished sections showed that some of the sulfate minerals have grown around and enclose relatively fresh pyrrhotite grains. We believe that the first step of the paragenesis at this site is when meteoric water and oxygen react with the pyrrhotite inside the rocks. The predominantly ferrous sulfate solution produced by pyrrhotite oxidation migrates to the wall of the pit, where it evaporates to form melanterite that subsequently dehydrates to rozenite. In the second step, the very fine-grained rozenite falls to the ground where it accumulates in piles. In the pile, some ferrous iron oxidizes to ferric iron. Finally, during wet times, some Fe^{2+}-Fe^{3+}-H_2SO_4 solution forms and migrates to sites of evaporation where copiapite grows as efflorescent blooms. During dry times, the reactions at Area II are probably slow. Halotrichite forms on top of copiapite as thin hair-like salts during very dry times. This reaction is probably driven by the high Al:Fe ratios that develop in the evaporating solutions as iron sulfate minerals form.

We have found that the mineral transformations described here involve oxidation reactions, hydration/dehydration reactions, and acidification/neutralization reactions. Of these, the first two reaction types seem to be the most important in con-

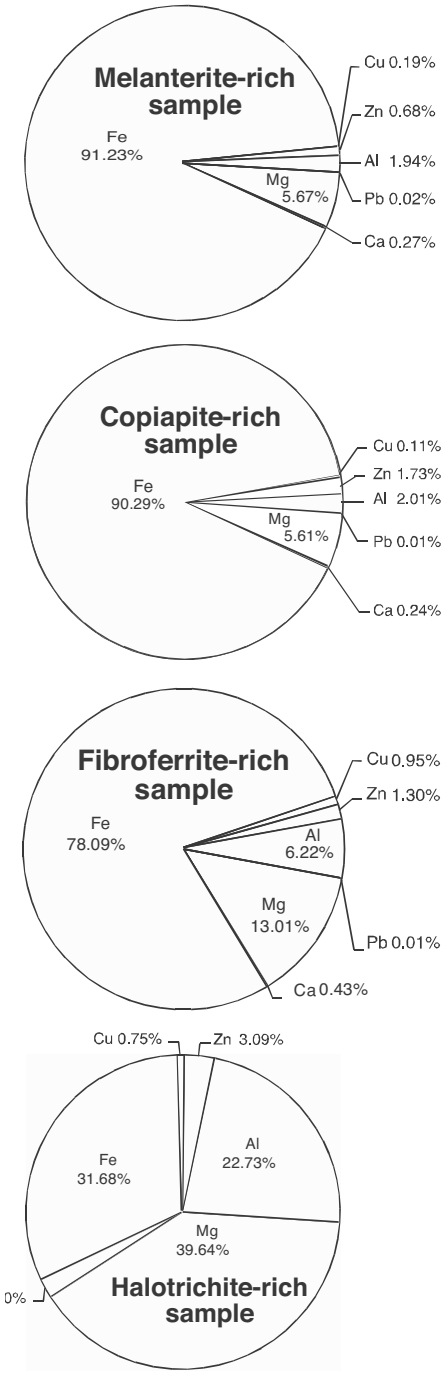

FIGURE 9. The relative cation abundances in solutions produced by dissolving the field samples. Concentrations are in mol% of total metals.

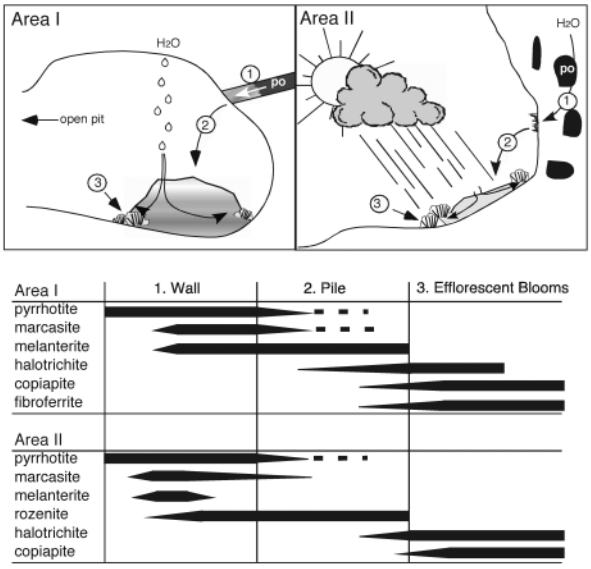

FIGURE 10. Schematic representation of the physical setting and paragenetic sequence in the two different sampling areas. Area I is located in an underground adit where the temperature and relative humidity are relatively constant; Area II is under an overhanging pit wall where the temperature and relative humidity vary significantly from time to time.

trolling the evolution of the mineralogy. The third process, acidification/neutralization, is driven by the production and consumption of sulfuric acid. For example, oxidation of pyrrhotite creates a small amount sulfuric acid (Eq. 2), albeit less than the oxidation of pyrite (Eq. 1), and subsequently sulfuric acid concentrations increase as ferrous sulfate-sulfuric acid rich solutions evaporate. Sulfuric acid is created or consumed in the subsequent transformation of sulfate phases and is important in the stability of some of the phases so it is also an important component of this system.

Activity Diagrams

A convenient way to visualize the relationships of the phases that we found at the Bumbarger and Iron King sites is with a log a_{O_2} – log a_{H_2O} diagram (Fig. 11). This diagram shows the chemical relationships of the phases that were identified in the field. The axes of this diagram were chosen to represent the two dominant reaction types controlling the iron sulfate paragenesis, oxidation and hydration/dehydration.

The chemical reaction that corresponds to each line on the diagram is listed in Table 5. In some cases, the position of the line could be calculated from published data. In other cases, thermodynamic properties of the phases are not known so that the exact location of the line on the diagram could not be determined. However, the slopes of the lines are controlled by the stoichiometry of the reaction and their position can be constrained using the field or laboratory observations made in this study. Dashed lines are used for the reactions where the slopes are known but we have very poor constraints on the actual position of the line.

Line A: Pyrrhotite and melanterite

The equilibrium between pyrrhotite and melanterite was calculated using ΔG_f^0 for troilite, oxygen, liquid water, and melanterite published in Robie and Hemingway (1995). Stoichiometric iron sulfide (troilite) is the most reduced form of

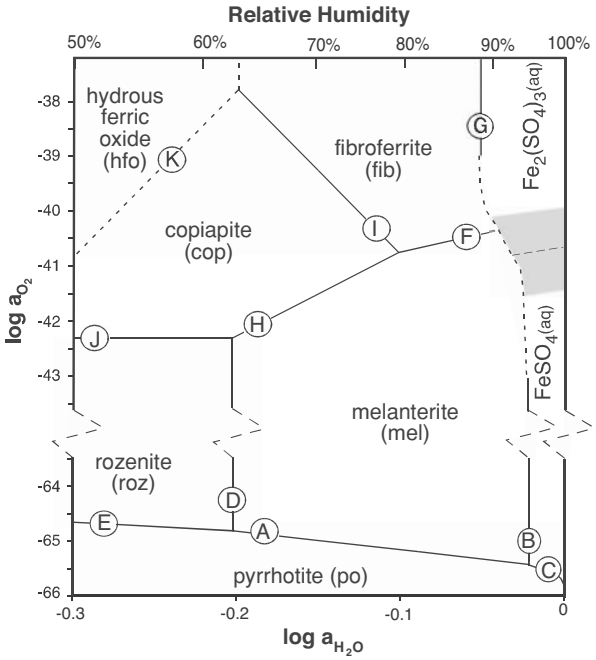

FIGURE 11. Log a_{O_2}-log a_{H_2O} diagram shows the relative stability of iron sulfide, sulfate, and oxyhydroxide phases. Letters by each phase boundary correspond to the reactions listed in Table 5. The shaded area indicates mixed $Fe_2(SO_4)_3$–$FeSO_4$ solutions.

pyrrhotite. Using the free energy of formation for pyrrhotite with a more sulfur-rich composition would shift the line to a slightly higher a_{O_2}, although not noticeably at the scale of this diagram. The reported values of ΔG_f^0 melanterite vary slightly in the literature [ΔG_f^0 = –2509.902 kJ/mol, DeKock 1982; ΔG_f^0 = –2509.5 kJ/mol, Robie and Hemingway 1995; –2509.87 kJ/mol, Wagman et al. (1982)]. We used the value from Robie and Hemingway (1995) for the sake of internal consistency.

Line B: Melanterite and solution

The dissolution of melanterite is independent of a_{O_2} and therefore plots as a vertical line on the diagram. Melanterite has been shown to deliquesce at a_{H_2O} = 0.952 (Linke 1958) or a_{H_2O} = 0.958 (Apelblat 1993). We used the latter value in our calculations. The difference between these values is too small to be visible on our diagram. However, this activity of water at melanterite saturation was used in other calculations.

The equilibrium between melanterite and solution was used to determine the placement of other lines on the diagram. Many studies of melanterite solubility, summarized by Linke (1958), have shown that the ferrous sulfate solution becomes saturated with respect to melanterite at a concentration of 1.96 molal. Reardon and Beckie (1987) used Pitzer equations to revise the data of Oykova and Balarew (1974) and determine the osmotic coefficient (used to determine the activity of water) and mean activity coefficient of $FeSO_4$ for various ferrous sulfate solution (Table 6). At 25 °C, the mean activity coefficient of fer-

TABLE 5. Chemical reactions and equations used to construct the log a_{O_2}-log a_{H_2O} (Fig. 11) and log $a_{H_2SO_4}$ – log a_{H_2O} (Fig. 12) diagrams. The slopes of all lines are shown in the equations and the intercepts are included when the equilibrium constant is known or can be calculated. The activity of sulfuric acid ($a_{H_2SO_4}$) on the log a_{O_2}-log a_{H_2O} is zero. Some phases whose formation involves sulfuric acid are projectioned onto the log a_{O_2}-log a_{H_2O} diagram from an unknown a_{H_2O}. Changes in a_{H_2O} will change the position of the lines when it is a product or reactant but will not change the slope.

no.	Balanced Reaction	Equation of Line
A	$FeS(po) + 2O_2 + 7H_2O = FeSO_4{\cdot}7H_2O(mel)$	$\log a_{O_2} = -\frac{7}{2}\log a_{H_2O} - 65.5$
B	$FeSO_4{\cdot}7H_2O(mel) = FeSO_4(aq) + 7H_2O$	$\log a_{H_2O} = -0.018$
C	$FeS(po) + 2O_2 = FeSO_4(aq)$	$\log a_{O_2} = -64.4 + 0.5\log a_{FeSO_4}$
D	$FeSO_4{\cdot}7H_2O(mel) = FeSO_4{\cdot}4H_2O(roz) + 3H_2O$	$\log a_{H_2O} = -0.222$
E	$FeS(po) + 2O_2 + 4H_2O = FeSO_4{\cdot}4H_2O(roz)$	$\log a_{O_2} = -2\log a_{H_2O} - 65.18$
F	$FeSO_4{\cdot}7H_2O(mel) + 1/4O_2 = Fe(OH)(SO_4){\cdot}5H_2O(fib) + 3/2H_2O$	$\log a_{O_2} = 6\log a_{H_2O} + 4\log K$
G	$2Fe(OH)(SO_4){\cdot}5H_2O(fib) + H_2SO_4 = Fe_2(SO_4)_3(aq) + 7H_2O$	$\log a_{H_2O} = -0.056$
H	$5FeSO_4{\cdot}7H_2O(mel) + H_2SO_4 + O_2 = FeFe_4(SO_4)_6(OH)_2{\cdot}20H_2O(cop) + 15H_2O$	$\log a_{O_2} = 15\log a_{H_2O} + \log K - \log a_{H_2SO_4}$
I	$FeFe_4(SO_4)_6(OH)_2{\cdot}20H_2O(cop) + 1/4O_2 + 15/2H_2O = 5Fe(OH)(SO_4){\cdot}5H_2O(fib) + H_2SO_4$	$\log a_{O_2} = -30\log a_{H_2O} + 4\log K + 4\log a_{H_2SO_4}$
J	$5FeSO_4{\cdot}4H_2O(roz) + H_2SO_4 + O_2 = FeFe_4(SO_4)_6(OH)_2{\cdot}20H_2O(cop)$	$\log a_{O_2} = \log K - \log a_{H_2SO_4}$
K	$FeFe_4(SO_4)_6(OH)_2{\cdot}20H_2O(cop) + 1/4\ O_2 = 5Fe(OH)_3(hfo) + 6H_2SO_4 + 15/2H_2O$	$\log a_{O_2} = 30\log a_{H_2O} + 4\log K + 24\log a_{H_2SO_4}$
L	$FeSO_4{\cdot}4H_2O(roz) + 1/4O_2 = Fe(OH)_3(hfo) + H_2SO_4 + 5/2H_2O$	$\log a_{O_2} = 10\log a_{H_2O} + 4\log K$
M	$FeS(po) + H_2SO_4 = FeS_2(py) + 3/2O_2 + H_2O$	$\log a_{H_2SO_4} = \log a_{H_2O} + \frac{3}{2}\log a_{O_2} + 78.83$
N	$FeS_2(py) + 7/2O_2 + 8H_2O = FeSO_4{\cdot}7H_2O(mel) + H_2SO_4$	$\log a_{H_2SO_4} = 8\log a_{H_2O} + \frac{7}{2}\log a_{O_2} + 210.0$
O	$FeS_2(py) + 7/2O_2 + H_2O = FeSO_4(aq) + H_2SO_4$	$\log a_{H_2SO_4} = \log a_{H_2O} + \frac{7}{2}\log a_{O_2} - 208.82 - \log a_{FeSO_4}$

rous sulfate at saturation is 0.048. We used this value to determine a_{FeSO_4} at saturation, as described by Nordstrom and Munoz (1994), and combined it with the updated value of a_{H_2O} at saturation to determine the equilibrium constant for reaction B:

$$K_B = \frac{a_{Fe} a_{SO_4} a_{H_2O}^7}{a_{melanterite}} = \frac{\left(m_{\pm_{FeSO_4}} \gamma_{\pm_{FeSO_4}}\right)^2 a_{H_2O}^7}{a_{melanterite}} = \frac{[(1.96)(0.048)]^2 (0.958)^7}{1} = 10^{-2.18} \quad (5)$$

Line C: Pyrrhotite and solution

The dissolution of pyrrhotite creates a ferrous sulfate solution and the activity of water decreases non-linearly as a function of the activity of the ferrous sulfate in solution, which is why the line is curved. The curve was calculated by first determining a_{O_2} where melanterite, pyrrhotite, and ferrous sulfate solutions coexist. To determine this value, the equilibrium constants for the reactions for lines A and B were multiplied to find the equilibrium constant for line C. Using this value (log K_c = –64.4), the equilibrium expression was solved to determine log a_{O_2} as a function of log a_{FeSO_4}:

$$\log a_{O_2} = -64.4 + 0.51 \log a_{FeSO_4} \quad (6)$$

This reaction is not represented by a horizontal line because the activity of water varies with the activity of ferrous sulfate in the solution. Using the activity coefficient of ferrous sulfate listed in Table 6, we calculated the activity of ferrous sulfate component in solution at various concentrations. Then, using the osmotic coefficient also listed in Table 6, we can calculate the activity of water using the following equation:

$$\log a_{H_2O} = \frac{-\nu m W_A}{(2.303)(1000)} \phi \quad (7)$$

TABLE 6. Osmotic (ϕ) and mean ionic activity coefficients ($\gamma_\pm$) for various concentrations (m) of ferrous sulfate in aqueous solutions

m_{FeSO_4}	ϕ	$\gamma_\pm$
0.1	0.556	0.161
0.2	0.515	0.115
0.3	0.511	0.093
0.4	0.509	0.081
0.5	0.519	0.073
0.6	0.521	0.067
0.7	0.527	0.062
0.8	0.532	0.059
0.9	0.542	0.056
1.0	0.547	0.054
1.1	0.557	0.052
1.2	0.562	0.051
1.3	0.574	0.050
1.4	0.584	0.049
1.5	0.598	0.048
1.6	0.617	0.047
1.7	0.636	0.047
1.8	0.657	0.047
1.9	0.685	0.048
2.0	0.705	0.049

Note: Activity coefficients are used to calculate activity of ferrous sulfate (line B) and the osmotic coefficients are used to calculate activity of water (line C) (Reardon and Beckie 1987).

where ν is the number of ions in the electrolyte (two for $FeSO_4$), m is the concentration of ferrous sulfate in the solution (mol/kg), W_A is the molecular weight of the solvent (18.0 g/mol for water), and ϕ is the osmotic coefficient (Robinson and Stokes 1959). The above equations were simultaneously used to determine a_{O_2} and a_{H_2O} in equilibrium with ferrous iron solutions as the concentration decreased away from melanterite saturation. The results of these calculations are listed in Table 7.

Line D: Melanterite and rozenite

This reaction is independent of a_{O_2} and therefore is a vertical line on the diagram. We used a value of activity of water in equilibrium with melanterite and rozenite, which is equal to 0.5998 based on the results reported by Chou et al. (2002).

Line E: Pyrrhotite and rozenite

The equilibrium constant for the line between rozenite and pyrrhotite was determined by multiplying the equilibrium constants for reactions A and D.

Line F: Melanterite and fibroferrite

The ΔG_f^0 of fibroferrite is unknown. Therefore, the equilibrium constant for this reaction cannot be determined. However, the slope of the line between these two phases is constrained by reaction stoichiometry to be six. In addition, we know that because fibroferrite contains only ferric iron and melanterite contains only ferrous iron, the melanterite/fibroferrite boundary must occur near a log a_{O_2} value where the solution has nearly equal amounts of ferrous and ferric iron. We can calculate the equilibrium constant for the oxidation of ferrous to ferric iron in dilute solutions and plot a line on the diagram where the activities of the two species are equal. This line, shown as a dashed, sub-horizontal line in the solution field on the diagram, has a slope of one and is pH dependent. At a pH of 2.5, log a_{O_2} equals –42. Therefore, we infer that the melanterite-fibroferrite reaction occurs near a log a_{O_2} of –42 as well.

Line G: Fibroferrite and Solution

Neither the ΔG_f^0 of fibroferrite nor the activity of the ferric iron in the saturated solution at equilibrium is known. So, we cannot calculate an equilibrium constant for this reaction. However, we can estimate where the line is located on the diagram. As previously discussed, we determined that fibroferrite deliquesces at a relative humidity of 88% (log a_{H_2O} of –0.055). This reaction is independent of oxygen and therefore plots as a vertical line on the diagram.

TABLE 7. The activity of oxygen and activity of water at various activities of ferrous sulfate solution in contact with pyrrhotite

log a_{FeSO_4}	log a_{O_2}	log a_{H_2O}
–1.793	–64.5	0.998
–1.495	–64.7	0.993
–1.318	–65.1	0.985
–1.124	–65.4	0.976
–1.018	–65.4	0.965
–1.027	–65.4	0.952

Line H: Melanterite and copiapite

The ΔG_f^0 of copiapite is unknown. However, from reaction stoichiometry, we can calculate that the slope of the phase boundary between copiapite and melanterite is +15. In addition, we measured the equilibrium relative humidity of copiapite plus solution to be 80% (log a_{H_2O} of –0.1) using the humidity buffer method. The copiapite field cannot lie to the right of this value. Furthermore, copiapite, fibroferrite, and melanterite were observed to coexist at the mine site. Therefore, the triple point between these three phases was placed at a log a_{H_2O} value of –0.01 and a log a_{O_2} value of –42.

Line I: Copiapite and Fibroferrite

The ΔG_f^0 values for these minerals are not known. However, they were observed to coexist at the mine site in Area I, suggesting that copiapite can oxidize to fibroferrite under humid conditions. We can write a reaction (I) and calculate that the slope of the line that describes this equilibrium is –30. In addition, we can constrain the placement of this line to the part of the diagram where $a_{H_2O} = 0.8$. Also, we observed melanterite, copiapite, and fibroferrite coexisting in the field. As previously discussed (line H), copiapite probably forms around the log a_{O_2} where concentrations of ferrous and ferric iron are equal in solution. This constrains the triple point between melanterite, copiapite, and fibroferrite to lie near log $a_{O_2} = –42$. The line between melanterite and fibroferrite extends from this triple point with a slope of six.

Line J: Copiapite and rozenite

Without the free energy of formation of copiapite, this equilibrium constant cannot be calculated. However, the line representing the reaction between copiapite and rozenite can be constrained by other considerations. The a_{H_2O} for melanterite and rozenite equilibrium has been carefully determined by Chou et al. (2002). We have already discussed the constraints on the line representing the reactions between melanterite and copiapite. By adding reaction D and H, we can calculate the slope of the line between copiapite and rozenite as zero so that it plots as a horizontal line that extends from the melanterite-rozenite-copiapite triple point.

Line K: Fibroferrite and iron oxyhydroxide

The iron oxyhydroxide phases found in the field were primarily amorphous. Therefore, we show the reaction between fibroferrite and metastable hydrous ferric oxide. This reaction does not involve any oxidation and therefore is a vertical line on the diagram. However, we do not know the activity of water where this transformation will take place, and therefore we cannot constrain its placement on the diagram. It is reasonable to assume that iron oxyhydroxide phases will eventually convert to goethite, the thermodynamically stable phase at a_{H_2O} greater than 0.41 (Langmuir 1997).

Line L: Copiapite and iron oxyhydroxide

Neither the activity of oxygen nor the activity of water at which copiapite oxidizes and dehydrates to iron oxyhydroxides is known. Therefore, it is very difficult to constrain the placement of this line. All we can presume is that it occurs at relatively high oxygen partial pressures and under relatively low relative humidity.

Stability of other sulfate phases

The log a_{O_2} – log a_{H_2O} diagram (Fig. 11) is constructed for the pure iron-sulfur system. Therefore, phases that contain other elements such as Al (halotrichite) or K (jarosite) do not plot on the diagram. We assume that halotrichite would occupy approximately the same field as melanterite, because they both contain ferrous iron and are fairly hydrous phases.

In addition, there is evidence that other mixed valence iron phases are present at our field site. These would project into the field that we have designated as copiapite. Copiapite is by far the most abundant mixed valence-state phase found at the mine site. Therefore, it is reasonable to conclude that it is stable over a range of $a_{O_2} – a_{H_2O}$ conditions. Note that the copiapite field is projected onto this diagram from an unknown activity of sulfuric acid.

Role of sulfuric acid

Sulfuric acid also plays an important role in the paragenesis of iron sulfate minerals. For example, the solubility of melanterite is reduced in H_2SO_4 solutions, and many of the reactions that form sulfate minerals that occur on the right hand side of Figure 1 involve consumption of sulfuric acid while the formation of iron oxyhydroxides produces sulfuric acid.

A good example of the role of sulfuric acid is its effect on the transformation of pyrrhotite to marcasite ± pyrite to melanterite. Reflected light observations of partly oxidized pyrrhotite show that an iron sulfide phase structurally similar to marcasite forms at the surface of the pyrrhotite grains (Blowes and Jambor 1990). The pyrrhotite grains collected from the Gossan Lead show that this process of forming iron disulfide by the partial oxidation of pyrrhotite occurs at our field site. Pyrrhotite, FeS_2, and melanterite coexist in these samples.

The oxidation of troilite to iron disulfide consumes sulfuric acid

$$FeS + H_2SO_4 = FeS_2 + {}^3/_2O_2 + H_2O \quad (8)$$

Equation 8 is written in terms of O_2 so that these phases can be described as a function of oxygen fugacity; we do not believe that this reaction will occur in nature because the rate of reduction of sulfate at low temperatures is too slow. FeS_2 is more likely produced by an alternative pathway described below.

The oxidation of iron disulfide to melanterite produces sulfuric acid:

$$FeS_2 + 7/2\ O_2 + 8\ H_2O = FeSO_4{\cdot}7H_2O + H_2SO_4 \quad (9)$$

Therefore, although the net reaction (reaction A) appears to be independent of sulfuric acid, it can also proceed step-wise as described by equations 8 and 9.

Figure 12 shows the stability of troilite, iron disulfide, melanterite, and solution as functions of the activity of sulfuric acid and the activity of water where the partial pressure of oxygen ranges from 10^{-67} to 10^{-63}. The lines on the diagrams correspond to the reactions listed in Table 5. Equilibrium constants

were calculated from free energy data compiled by Robie and Hemingway (1995) except for the free energy of sulfuric acid. We used a 1.0 molal ideal solution for the reference state of sulfuric acid ($\Delta G_f^0 = -744.53$) (Wagman et al. 1982). For reactions involving iron disulfide, we used the free energy of formation for marcasite because it is likely that the alteration phase is very similar to marcasite. Using the free energy of formation of pyrite would cause an imperceptible increase in the size of the FeS_2 field. The activity of water in a ferrous sulfate-sulfuric acid solution at melanterite saturation was calculated using the Pitzer method. The activity of H_2SO_4 is too low in these solutions to affect a_{H_2O}. The activity of ferrous sulfate solution was calculated using the parameters in Table 6.

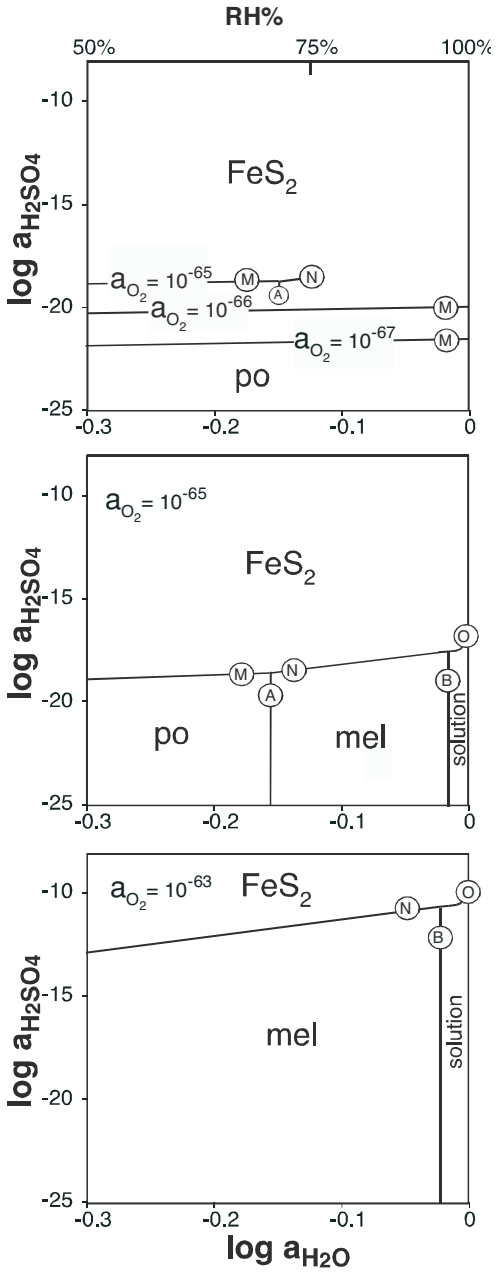

FIGURE 12. Log$a_{H_2SO_4}$-log a_{H_2O} diagram showing the relative stability of pyrrhotite, FeS_2, melanterite, and solution at different partial pressures of oxygen. The top diagram shows how the pyrrhotite-FeS_2 boundary moves to higher H_2SO_4 activities as the O_2 activity increases. When the O_2 activity reaches between 10^{-66} and 10^{-65} fields for melanterite and coexisting solution appear to create the topology shown in the middle diagram. The bottom diagram shows that increasing the O_2 activity to 10^{-63} causes the melanterite field to expand significantly at the expense of the pyrrhotite and FeS_2 fields. The melanterite field enlarges very quickly with increasing O_2 activity. Letters by each phase boundary correspond to the reactions listed in Table 5.

At very low oxygen partial pressures (10^{-67}–10^{-65}), only pyrrhotite and iron disulfide are stable and no ferrous sulfate solution is present. When log a_{O_2} increases to –65, the equilibrium between pyrrhotite and iron disulfide moves toward higher activities of sulfuric acid. When log $a_{O_2} = -65.3$ (not shown), the ferrous sulfate solution and melanterite fields begin to grow out of the pyrrhotite field. The equilibrium activity of water set by the pyrrhotite to melanterite reaction decreases with increasing log a_{O_2}. This can also be seen on the log a_{O_2} – log a_{H_2O} diagram (Fig. 11). With further increases of a_{O_2}, the triple point between pyrrhotite, iron disulfide, and melanterite moves up and to the left. When the partial pressure of oxygen rises to 10^{-63}, pyrrhotite is no longer present on the diagram and the equilibrium between melanterite and marcasite increases to higher activities of sulfuric acid. Further increase in a_{O_2} will cause melanterite to grow at the expense of FeS_2 until the entire diagram consists of either melanterite or solution.

Intermediate hexagonal pyrrhotite ($Fe_{0.9}S$) occurs at our field site so FeS_2 can be produced by a different reaction than equation (8). In this case, $a_{H_2SO_4}$ is not set externally, but rather the H_2SO_4 comes from the oxidation of the pyrrhotite (equation 4). This sulfuric acid reacts with pyrrhotite to generate FeS_2 and melanterite:

$$2Fe_{1-x}S + (1 - 2x)H_2SO_4 + (6 - x)H_2O = FeS_2 + (1 - x)FeSO_4 \cdot 7H_2O \quad (10)$$

Oxidation of FeS_2 to melanterite also generates additional sulfuric acid so this is a self-perpetuating reaction. These reactions occur at the triple point between pyrrhotite, FeS_2, and melanterite (Fig. 12). With increasing a_{O_2} this triple point migrates to lower a_{H_2O} and higher $a_{H_2SO_4}$.

Sulfuric acid is also important for reactions involving ferric-bearing sulfate minerals on the log a_{O_2} – log a_{H_2O} diagram. For example, the formation of copiapite from melanterite (reaction H, Table 5) consumes H_2SO_4. Unfortunately, neither the free energy of formation of the minerals nor the thermodynamic properties of ferric sulfate-sulfuric acid solutions are known. A change in the activity of sulfuric acid will cause the stability fields of ferric-bearing sulfate minerals to change as well. The fields shown at high log a_{O_2} on the log a_{O_2} – log a_{H_2O} diagram (Fig. 11) are estimated from our field observations. We know that some H_2SO_4 is present, so the stability field of copiapite is a projection onto the log a_{O_2} – log a_{H_2O} surface from $a_{H_2SO_4} > 0$.

DISCUSSION

We can combine our paragenesis observation (Fig. 10) with the log a_{O_2} – log a_{H_2O} diagram (Fig. 11) to create a reaction path that explains our observations at the sites. At Area I, the reac-

tion pathway moves from the pyrrhotite-melanterite-solution triple point, through the melanterite field, into the copiapite field near the triple point between melanterite-copiapite-fibroferrite, then into the fibroferrite field, and finally into the iron oxyhydroxide field. At Area II, the reaction path moves from the pyrrhotite-melanterite-solution triple point, into the melanterite field, and then into the rozenite field, before moving into the copiapite field and finally into the iron oxyhydroxide field.

These paths reflect the differing field conditions, which control the rate of transformation of the minerals. For example, the relative humidity of Area I is consistently high. Therefore, we expect that oxidation reactions proceed faster than dehydration reactions. By contrast, in the low relative humidity of Area II, minerals dehydrate faster than they oxidize. Oxidation may proceed more rapidly in Area II during rain events or times of higher ambient relative humidity.

Water Quality Effects

Results from the dissolution experiments show that all the sulfate mineral samples will release acid and trace metals upon dissolution. However, the impact of each phase is different. Phases bearing trivalent cations (fibroferrite, copiapite, halotrichite) release the most acid due to the extensive hydrolysis of ferric iron and/or aluminum. Ferrous iron also undergoes hydrolysis, but to a lesser extent so that melanterite solutions are less acidic. However, when aqueous ferrous iron oxidizes to ferric iron, further hydrolysis will occur. Therefore, Fe^{2+}-bearing phases (melanterite, rozenite, copiapite, halotrichite), produce some immediate acidity and some latent acidity. The difference between the acid producing potential of sulfate minerals is most marked in very dilute solutions. In moderately concentrated solutions (>1 wt%), the pH of the leachate solutions was less than 3.0 for all minerals from the site.

All the field samples contained metals besides iron. The most abundant metals were magnesium, aluminum, zinc, copper, calcium, and lead. The molar concentrations of the metals varied with mineralogy. The melanterite-rich sample contained the least amount of associated metals, although it did contain the most lead. Magnesium was the second most abundant metal after iron in the leachate of all the field samples except halotrichite-rich one. In the halotrichite-rich field sample, magnesium was the most important cation, followed by iron, then aluminum. Not surprisingly, halotrichite-rich samples contained a high proportion of aluminum (23% of all metals on a molar basis). The mineralogy of these samples probably lie within the solid solution between halotrichite and pickeringite, the magnesium end-member. The fibroferrite-rich sample also contained a significant amount of aluminum (6 mol% of all metals). All samples released some measurable lead upon dissolution. Lead concentrations in the resulting solutions will depend on the water:rock ratio of the dissolution, but in these experiments where the ratio was approximately 20:1, they were up to 500 ppb. The host mineral for the lead is unknown.

The fibroferrite-rich sample released the most acid upon dissolution and contains the most associated trace metals of the sulfate phases found at the field site. However, it dissolved more slowly than the other phases. The halotrichite-rich sample also released significant acid and the most aluminum upon dissolution and it dissolved faster. These two samples would have the highest potential to impact the quality of receiving waters at this site. The copiapite-rich sample produced a significant amount of acid, but did not contain as many potentially toxic metals as the other two samples. The melanterite-rich sample produced the least amount of acid and the least amount of trace metals upon dissolution. Therefore, of the samples from this site, the melanterite-rich one appears to be the most benign.

Acknowledgments

We appreciate the help of J. Hammarstrom and N. Piatak in the identification of the sulfate minerals. In addition, our interpretations were aided by discussions with the former individuals. We are also grateful for the assistance of H. Shannon in the field, with the humidity cell experiments, and with the acid generation experiments. This manuscript benefitted from the comments of J. Craig, P. Dove, L. Daniels, and K. Nordstrom. We thank J.L. Jambor and I-M. Chou for their exceptionally thorough and useful reviews of the manuscript. This project was funded by a grant from the NSF (EAR-0003364), the Waste Policy Institute at Virginia Tech, and the Graduate Student Association at Virginia Tech.

References cited

Alpers, C.N., Nordstrom, D.K., and Thompson, J.M. (1994) Seasonal variations of Zn/Cu ratios in acid mine water from Iron Mountain, California. In C.N. Alpers and D.W. Blowes, Eds., 204th National Meeting of the American Chemical Society, p. 324–344. American Chemical Society, Washington D.C.

Apelblat, A. (1993) The vapour pressure of saturated aqueous solution of potassium bromide, ammonium sulfate, copper(II) sulfate, iron(II) sulfate, and manganese(II) dichloride, at temperatures from 283 K to 308 K. Journal of Chemical Thermodynamics, 25, 1513–1520.

Bandy, M.C. (1938) Mineralogy of three sulphate deposits of northern Chile. American Mineralogist, 23, 669–760.

Bayless, E.R. and Olyphant, G.A. (1993) Acid-generating salts and their relationship to the chemistry of groundwater and storm runoff at an abandoned mine site in southeastern Indiana, USA. Journal of Contaminant Hydrology, 12, 313–328.

Blowes, D.W. and Jambor, J.L. (1990) The pore-water geochemistry and the mineralogy of the vadoze zone of sulfide tailings, Waite-Amulet, Quebec, Canada. Applied Geochemistry, 5, 327–346.

Bol'shakov, A.P. and Ptushko, L.I. (1971) Alteration products of melanterite from Nikitov mercury ore deposits. International Geology Review, 13, 849–854.

Buurman, P. (1975) In vitro weathering products of pyrite. Geologie en Mijnbouw, 54, 101–105.

Chou, I.-M., Seal, R.R., and Hemingway, B.S. (2002) Determination of melanterite-rozenite and chalcanthite-bonattite equilibria humidity by measurements at 0.1 MPa. American Mineralogist, 87, 108–114.

Craig, J.R. (1980) Stratiform sulfide mineralization in the central U.S. Appalachians. Norges Geologiske Undersøkelse, 360, 57–84.

Cravotta, C.A.I. (1994) Secondary iron-sulfate minerals as sources of sulfate and acidity. In C.N. Alpers, and D.W. Blowes, Eds., 204th National Meeting of the American Chemical Society, p. 345–364. American Chemical Society, Washington D.C.

Dagenhart Jr., T.V. (1980) The acid mine drainage of Contrary Creek, Louisa County, Virginia: Factors causing variations in stream water chemistry. M.S. Thesis, University of Virginia.

DeKock, C.W. (1982) Thermodynamic Properties of Selected Transition Metal Sulfates and their Hydrates. U.S. Bureau of Mines Information Circular 8910. 45 pp.

Frau, F. (2000) The formation-dissolution-precipitation cycle of melanterite at the abandoned pyrite mines of Genna Luas in Sardinia, Italy: environmental implications. Mineralogical Magazine, 64, 995–1006.

Gair, J.E. and Slack, J.F. (1984) Deformation, geochemistry, and origin of massive sulfide deposits, Gossan Lead District, Virginia. Economic Geology, 79, 1483–1520.

Greenspan, L. (1977) Humidity fixed points of binary saturated aqueous solutions. Journal of Research of the National Bureau of Standards-A. Physics and Chemistry, 81A, 89–96.

Haar, L., Gallager, J.S., and Kell, G.S. (1984) NBS/NRC Steam Tables, Hemisphere Publishing Corp., New York. 320 pp.

Henry, D.K., Craig, J.R., and Gilbert, M.C. (1979) Ore mineralogy of the Great Gossan Lead, Virginia. Economic Geology, 74, 645–656.

Jambor, J.J., Nordstrom, D.K., and Alpers, C.N. (2000) Metal-sulfate salts from sulfide mineral oxidation. In C.N. Alpers, J.L. Jambor, and D.K. Nordstrom, Eds., Sulfate Minerals: Crystallography, Geochemistry, and Environmental Significance, 40, p. 303–350. Mineralogical Society of America and Geochemical Society, Washington, D.C.

Jerz, J.K. (1998) Mechanisms of Acid and Metal Release from a Fluvial Tailings Deposit. Geochemistry, p. 133. M.S. thesis Colorado School of Mines, Golden, Colorado.

——— (2002) Geochemical Reactions in Unsaturated Mine Wastes. Ph.D. dissertation. Virginia Polytechnic Institute and State University. 95 pp.

Keith, D.C., Runnels, D.D., Esposito, K.J., Chermak, J.A., and Hannula, S.R. (1999) Efflorescent sulfate salts-Chemistry, mineralogy, and effects of ARD streams. The Sixth International Conference on Tailings and Mine Waste '99, p. 573–579. Balkema, Rotterdam, Fort Collins, Colorado.

Keith, D.C., Runnells, D.D., Esposito, K.J., Chermak, J.A., Levy, D.B., Hannula, S.R., Watts, M., and Hall, L. (2001) Geochemical models of the impact of acidic groundwater and evaporative sulfate salts on Boulder Creek at Iron Mountain, California. Applied Geochemistry, 16, 947–961.

Langmuir, D. (1997) Aqueous Environmental Geochemistry. 600 p. Prentice Hall, Upper Saddle River, New Jersey.

Linke, W.F. (1958) Ferric Sulfate $Fe_2(SO_4(SO_4)_3$. Solubilities: Inorganic and Metal-Organic Compounds, 1, 1058–1064. Van Nostrand Company, Inc., Princeton.

McKibben, M.A. and Barnes, H.L. (1986) Oxidation of pyrite in low temperature acidic solutions: rate laws and surface textures. Geochimica et Cosmochimica Acta, 50, 1509–1520.

Nordstrom, D.K. and Alpers, C.N. (1999) Geochemistry of acid mine waters. In G.S. Plumlee and M.J. Logsdon, Eds., The Environmental Geochemistry of Mineral Deposits, 6A, p. 131–160. Society of Economic Geologists, Inc., Littleton, Colorado.

Nordstrom, D.K. and Munoz, J.L. (1994) Geochemical Thermodynamics. 493 p. Blackwell Scientific Publications, Boston.

Oykova, T.G. and Balarew, C. (1974) Thermodynamic study of magnesium sulfate-ferrosulfate-water system at 25°C. Comptes Rendus de l'Academie Bulgare des Sciences, 27, 1211–1214.

Powder Diffraction File (PDF) (2000) International Center for Diffraction Data, Newtown Square, Pennsylvania. <http://www.icdd.com>

Rankin, D.W., Espenshade, G.H., and Shaw, K.W. (1973) Stratigraphy and structure of the metamorphic belt in the northwestern North Carolina and southwestern Virginia: A study from the Blue Ridge across the Brevard zone to the Sauratown Mountains anticlinorium. American Journal of Science, 273A, 1–40.

Reardon, E.J. and Beckie, R.D. (1987) Modeling chemical equilibria of acid mine-drainage: The $FeSO_4$-H_2SO_4-H_2O system. Geochimica et Cosmochimica Acta, 51, 2355–2368.

Robie, R.A. and Hemmingway, B.S. (1995) Thermodynamic properties of minerals and related substances at 298.15 K and 1 bar (10^5 pascals) pressure and at higher temperatures. U.S. Geological Survey, Washington, D.C.

Robinson, R.A. and Stokes, R.H. (1959) Electrolyte Solutions 2nd ed. Academic, New York.

Singer, P.C. and Stumm, W. (1970) Acidic mine drainage: The rate-determining step. Science, 163, 1121–1123.

Staten, W.T. (1976) A chemical study of the silicate minerals of the Gossan Lead and surrounding rocks in southwestern Virginia. Geological Sciences, p. 110. Virginia Polytechnic Institute and State University, Blacksburg. Virginia.

Stewart, B.R., Daniels, W.L., and Jackson, M.L. (1997) Evaluation of leachate quality from the co-disposal of coal fly ash and coal refuse. Journal of Environmental Quality, 26, 1417–1424.

Stose, A.J. and Stose, G.W. (1957) Geology and Mineral Resources of the Gossan Lead District and Adjacent Areas in Virginia. Virginia Division of Mineral Resources, Charlottesville, Virginia.

Wagman, D.D., Evans, W.H., Parker, V.B., Schumm, R.H., Halow, I., Bailey, S.M., Churney, K.L., and Nuttal, R.L. (1982) The NBS tables of chemical thermodynamic properties. Selected values for inorganic and C_1 and C_2 organic substances in SI unites. Journal of Physical and Chemical Reference Data, 11(Supplement No. 2), 2–58.

Williamson, M.A. and Rimstidt, J.D. (1994) The kinetics and electrochemical rate-determining step of aqueous pyrite oxidation. Geochimica et Cosmochimica Acta, 58, 5443–5454.

Young, J.F. (1967) Humidity control in the laboratory using salt solutions—a review. Journal of Applied Chemistry, 17, 241–245.

Zodrow, E.L., Wiltshire, J., and McCandlish, K. (1979) Hydrated sulfates from Sydney Coalfield, Cape Breton Island, Nova Scotia. II. Pyrite and its alteration products. Canadian Mineralogist, 17, 63–70.

MANUSCRIPT RECEIVED JULY 23, 2002
MANUSCRIPT ACCEPTED FEBRUARY 3, 2003
MANUSCRIPT HANDLED BY LEE GROAT